*J. Fluid Mech.* (2006), *vol.* 553, *pp.* 227–252. © 2006 Cambridge University Press 
doi:10.1017/S0022112006008810 Printed in the United Kingdom

# On the flow past a magnetic obstacle

By SERGIO CUEVAS†, SERGEY SMOLENTSEV AND MOHAMED A. ABDOU

Mechanical and Aerospace Engineering Department, University of California, Los Angeles, 44-114 Engineering IV, Los Angeles, CA 90095-1795, USA

(Received 19 May 2004 and in revised form 1 November 2005)

This paper analyses numerically the quasi-two-dimensional flow of an incompressible electrically conducting viscous fluid past a localized zone of applied magnetic field, denominated a *magnetic obstacle*. The applied field is produced by the superposition of two parallel magnetized square surfaces, uniformly polarized in the normal direction, embedded in the insulating walls that contain the flow. The area of these surfaces is only a small fraction of the total flow domain. By considering inertial effects in the analysis under the low magnetic Reynolds number approximation, it is shown that the flow past a magnetic obstacle may develop vortical structures and eventually instabilities similar to those observed in flows interacting with bluff bodies. In the small zone where the oncoming uniform flow encounters the non-negligible magnetic field, the induced electric currents interact with the field, producing a non-uniform Lorentz force that brakes the fluid and creates vorticity. The effect of boundary layers is introduced through a friction term. Due to the localization of the applied magnetic field, this term models either the Hartmann braking within the zone of high magnetic field strength or a Rayleigh friction in zones where the magnetic field is negligible. Finite difference numerical computations have been conducted for Reynolds numbers $Re = 100$ and 200, and Hartmann numbers in the range $1 \leqslant Ha \leqslant 100$ ($Re$ and $Ha$ are based on the side length of the magnetized square surfaces). Under these conditions, a wake is formed behind the obstacle. It may display two elongated streamwise vortices that remain steady as long as the Hartmann number does not exceed a critical value. Once this value is reached, the wake becomes unstable and a vortex shedding process similar to the one observed in the flow past bluff bodies is established. Similarities and differences with the flow around solid obstacles are discussed.

## 1. Introduction

The effect of a uniform magnetic field on the flow around solid obstacles has attracted the attention of many researchers since the pioneering works by Stewartson (1956) and Ludford (1960). Kolesnikov & Tsinober (1972) observed that vortices created due to an array of cylindrical obstacles in the presence of a strong magnetic field aligned their axes in the field direction. Recently, Mück *et al.* (2000) have carried out an extensive numerical study of the magnetohydrodynamic (MHD) flow around a square cylinder placed in an insulated rectangular duct. They investigated the formation and transport of vortices under the influence of a uniform magnetic field aligned with the cylinder. This flow was also studied experimentally by Frank, Barleon & Müller

† Present address: Centro de Investigación en Energía, UNAM, A. P. 34, Temixco, Mor. 62580, México.

https://doi.org/10.1017/S0022112006008810 Published online by Cambridge University Press

(2001), who addressed the onset of time-dependent vortex shedding. These studies have confirmed the well-known tendency of this kind of MHD flow to become quasi-two-dimensional. The vortices in the wake behind the obstacle evolved to have their axes aligned with the magnetic field while they were damped out in the boundary layers due to Hartmann braking. However, the effect of non-uniform fields in MHD flows with or without solid obstacles has not been widely explored. Most of the studies that deal with flows in non-uniform fields are restricted to duct flows with a field that varies in the streamwise direction such as, for instance, flows at the entrance or exit of the poles of a magnet (e.g. Lavrent'ev *et al.* 1990; Sterl 1990; Ting *et al.* 1993; Sellers & Walker 1999). As it will be shown in this paper, the flow of a conducting fluid passing a localized zone of applied magnetic field exhibits some features similar to those observed in ordinary flows around solid obstacles. In order to emphasize the analogy with this kind of flow, we introduce the term *magnetic obstacle* to describe the obstruction found by the fluid as it moves through a zone of localized non-uniform magnetic field.

The flow of conducting fluids in non-uniform magnetic fields is of interest in many technological applications. For instance, blanket designs in Tokamak toroidal confinement fusion systems rely on knowledge of the flow dynamics and heat transfer of conducting liquids under strong non-uniform magnetic fields (Abdou *et al.* 2001). Although steady models of fusion MHD flows grasp many important features, unsteady flow analysis is required to provide realistic simulations for design purposes. However, most of the studies devoted to the analysis of fusion MHD flows are based on stationary inertialess assumptions. The rationale of this approach lies in the hope that under fusion operation conditions, a suppression of time-dependent inertial flows by magnetic damping could occur. However, this might not be the case and, in fact, the promotion of non-steady inertial flows is even desirable for heat transfer enhancement purposes (Reed & Picologlou 1989; Bühler 1996; Burr *et al.* 2000; Mück *et al.* 2000).

Vortices can be generated in MHD flows without solid obstacles. In pressure-driven duct flows, vorticity can be created under fringing fields or through an expansion or contraction in a uniform field (e.g. Sellers & Walker 1999; Walker & Picologlou 1995). The destabilization of the side layer jets attached to the sidewalls parallel to the magnetic field of a rectangular conducting duct has also been observed (Reed & Picologlou 1989; Burr *et al.* 2000). Several works of particular relevance for the present investigation have shown that the existence of electromagnetic non-uniformities in the flow, which can be considered as *electromagnetic obstacles*, may promote the generation of internal shear layers and the appearance of flow instabilities when inertial effects are not negligible. Alpher *et al.* (1960) studied experimentally the shallow flow of mercury in an insulating open channel in which a copper disk much thinner than the fluid depth was mounted on the bottom. They observed a stagnation zone above the disk so that the flow acted as if a solid cylinder were immersed in the flow. They also observed the formation of a Kármán vortex street in the wake of the disk. In turn, in a theoretical study Bühler (1996) investigated a quasi-two-dimensional flow in a flat channel with non-uniform electrical wall conductivity under a strong uniform magnetic field. He was able to show that inhomogeneity in the wall conductivity may develop an instability that leads to time-dependent solutions similar to the Kármán vortex street behind bluff bodies. On the other hand, in an experiment shown by Shercliff (1965) in an educational film, a layer of mercury at rest is placed in between the poles of a magnet. As the magnet is moved manually, a vortex-type flow develops in the zone affected by the magnetic field and a wake is created.

https://doi.org/10.1017/S0022112006008810 Published online by Cambridge University Press

Honji (1991) and Honji & Haraguchi (1995) performed experimental studies on the flow induced by the interaction of a localized moving magnetic field with an electric current applied through a thin layer of salt water. In Honji (1991) two permanent magnets were located externally so that a small zone of the layer was between a north–south pole magnetic field. The magnets were moved at a constant velocity along the centreline of a water tank while a steady electric current was imposed on the fluid layer transversally to the motion of the magnets. Depending on the velocity of the magnet pair and the imposed electric current, Honji observed a wavy motion in the far wake behind the region influenced by the field. In Honji & Haraguchi (1995) a single moving magnet was placed on the bottom of the tank and attention was focused on the near wake. Steady symmetric vortex pairs were observed in a limited range of Reynolds numbers and Lorentz force intensities. As the Lorentz force increased, the symmetric vortex pair collapsed to form an unsteady periodic Kármán-like flow. In works by Alpher *et al.* (1960) and Bühler (1996) internal shear layers were created by non-uniform electrical boundary conditions at the channel walls. In contrast, in the experiments by Shercliff (1965), Honji (1991) and Honji & Haraguchi (1995) shear layers were promoted by localized gradients of magnetic field.

In this paper, we investigate the production of vorticity by Lorentz forces in a low magnetic Reynolds number flow without solid obstacles. We use a fully numerical approach to analyse the quasi-two-dimensional flow of a conducting incompressible viscous fluid in a zone where a localized magnetic field source, produced by two small magnetized square surfaces, exists. Unlike Honji's experiments, the flow is not influenced by applied electric currents. The main interest is to investigate the possibility of generating steady and unsteady vortices due to localized magnetic field gradients.

## 2. Formulation

We consider the flow of an electrically conducting incompressible viscous fluid between two rigid insulating parallel walls under an applied non-uniform magnetic field, $\boldsymbol{B}^0 = \boldsymbol{B}^0(x, y, z)$. The field is created by the superposition of two magnetized insulating rectangular surfaces uniformly polarized in the normal direction, for which an explicit analytical expression is available (McCaig 1977). The surfaces are placed opposite each other, embedded on the bottom and top walls with opposing polarization axes (see figure 1*a*). In this way, although a three-dimensional field exists in the fringing regions, the dominant contribution of the applied field comes from the component normal to the walls that lies along the $z$-direction. Due to its fast decay, the field presents high intensity only in a localized zone which is assumed to be distant from the inlet/outlet region as well as from the lateral boundaries. At the entrance, a steady unidirectional flow with a uniform velocity is imposed in the positive $x$-direction. Far from the region of intense field the flow is undisturbed. The motion of the fluid within the applied field induces electric currents which, in turn, generate an induced field $\boldsymbol{b}$, so that the total magnetic field is given by $\boldsymbol{B} = \boldsymbol{B}^0 + \boldsymbol{b}$. Since the confining walls are assumed to be electrically insulated, electric currents form closed loops within the fluid. Some cross-sectional currents (in the $y, z$-plane) are closed near the walls through Hartmann layers formed due to the normal field component, mostly in the zone of high-field intensity. However, current loops are also formed in planes parallel to the walls (in the $x, y$-plane), as will be discussed below. The latter interact with the magnetic field, giving rise to a non-uniform Lorentz force that brakes the fluid flow and creates vorticity in the bulk. In turn, Hartmann braking, generated due to cross-sectional loops, tends to stabilize the flow. The global effect is

https://doi.org/10.1017/S0022112006008810 Published online by Cambridge University Press

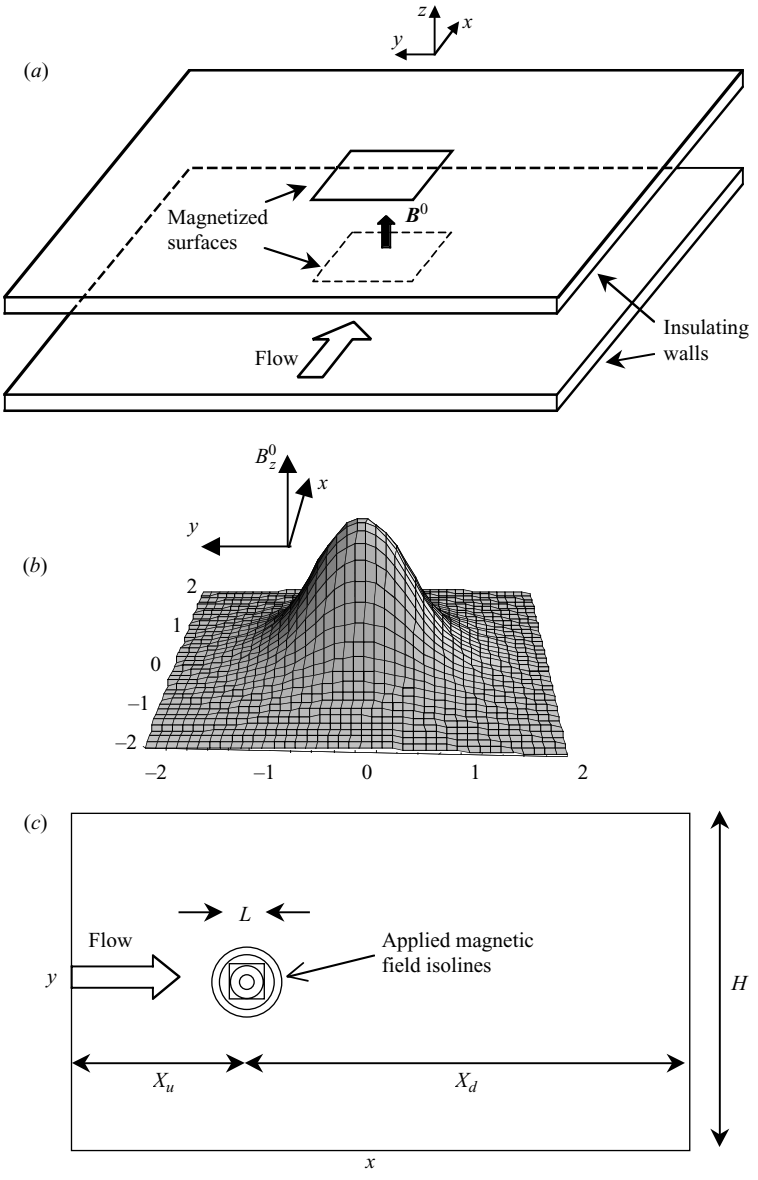



FIGURE 1. (*a*) Sketch of the magnetic obstacle flow problem. (*b*) Applied magnetic field distribution in the bulk flow. (*c*) Geometrical parameters and flow configuration.

that the localized magnetic field acts as an obstacle for the flow. Unlike solid obstacles that occupy a defined space region, the magnetic obstacle has an appreciable influence not only in the zone covered by the magnetized surfaces but also beyond their edges in what we call here the *fringing zones*. When referring to the magnetic obstacle, both the fringing zones and the area covered by the magnetized surfaces are considered. Although this is not a strict definition, the magnetic obstacle is identified as the zone where all the flow variables experience significant variations. Notice that the characteristic size of the magnetic obstacle, and consequently the extent of the region where the flow is substantially altered, is not determined only by the dimensions of

https://doi.org/10.1017/S0022112006008810 Published online by Cambridge University Press

the magnetized surfaces but also depends, for a given fluid, on the magnetic field strength and the oncoming flow velocity.

In this work, the problem is formulated using the flow velocity, the pressure and the induced magnetic field, assuming the induced field to be much smaller than the applied field, $\boldsymbol{b} \ll \boldsymbol{B}^0$. In terms of dimensionless parameters, this implies that the magnetic Reynolds number, $Rm = \mu\sigma U L$, is much less than unity, a condition that holds in most laboratory and industrial flows with liquid metals, molten salts and electrolytes. Here, $\mu$ and $\sigma$ are the magnetic permeability and the electrical conductivity of the fluid, respectively, $U$ is the undisturbed velocity at the entrance of the integration domain and $L$ is a characteristic length. Under the approximation $Rm \ll 1$, the governing equations of motion in dimensionless form are

$$\nabla \cdot \boldsymbol{u} = 0, \tag{2.1}$$

$$\frac{\partial \boldsymbol{u}}{\partial t} + (\boldsymbol{u} \cdot \nabla)\boldsymbol{u} = -\nabla p + \frac{1}{Re}\nabla^2 \boldsymbol{u} + \frac{Ha^2}{Re}\boldsymbol{j} \times \boldsymbol{B}^0, \tag{2.2}$$

where the velocity $\boldsymbol{u}$, the pressure $p$, the electric current density $\boldsymbol{j}$, and the applied field $\boldsymbol{B}^0$ are normalized by $U$, $\rho U^2$, $\sigma U B_{max}$ and $B_{max}$, respectively, where $\rho$ is the mass density of the fluid and $B_{max}$ is the maximum magnetic field strength. Dimensionless coordinates $x$, $y$ and $z$ are all normalized by $L$ while time $t$ is normalized by $L/U$. Notice that in equation (2.2) the contribution of $\boldsymbol{b}$ to the Lorentz force has been neglected. In addition, the dimensionless parameters

$$Ha = B_{max} L \sqrt{\frac{\sigma}{\rho \nu}}, \qquad Re = \frac{UL}{\nu} \tag{2.3}$$

stand for the Hartmann and Reynolds numbers, respectively, where $\nu$ is the kinematic viscosity of the fluid. The Hartmann number squared gives an estimate of magnetic forces compared to viscous forces while the Reynolds number denotes the ratio of inertia and viscous forces. The Hartmann and Reynolds numbers can be combined to form the interaction parameter $N = Ha^2/Re$, which represents the ratio of magnetic forces and inertia forces.

The electromagnetic equations in the MHD approximation (Moreau 1990) are

$$\nabla \times \boldsymbol{E} = -\frac{\partial \boldsymbol{B}}{\partial t}, \qquad \nabla \times \boldsymbol{B} = Rm\,\boldsymbol{j}, \tag{2.4}$$

$$\nabla \cdot \boldsymbol{B} = 0, \qquad \boldsymbol{j} = \boldsymbol{E} + \boldsymbol{u} \times \boldsymbol{B}, \tag{2.5}$$

where the electric field $\boldsymbol{E}$ is normalized by $U B_{max}$. Equations (2.4) and (2.5) can be combined to give the so-called induction equation (Moreau 1990). If the assumption $\boldsymbol{B} = \boldsymbol{B}^0 + Rm\boldsymbol{b}$ is made, the induction equation is

$$Rm\frac{\partial \boldsymbol{b}}{\partial t} = \nabla^2 \boldsymbol{b} + (\boldsymbol{B}^0 \cdot \nabla)\boldsymbol{u} - (\boldsymbol{u} \cdot \nabla)\boldsymbol{B}^0 + Rm(\boldsymbol{b} \cdot \nabla)\boldsymbol{u} - Rm(\boldsymbol{u} \cdot \nabla)\boldsymbol{b}, \tag{2.6}$$

where the induced magnetic field $\boldsymbol{b}$ is normalized by $Rm B_{max}$. Under the approximation $Rm \ll 1$, the induction equation reduces to its quasi-static form, namely,

$$\nabla^2 \boldsymbol{b} + (\boldsymbol{B}^0 \cdot \nabla)\boldsymbol{u} - (\boldsymbol{u} \cdot \nabla)\boldsymbol{B}^0 = 0. \tag{2.7}$$

The induced field implicitly satisfies the equations

$$\nabla \cdot \boldsymbol{b} = 0, \qquad \nabla \times \boldsymbol{b} = \boldsymbol{j}. \tag{2.8a, b}$$

In practice, Ampere's law (2.8$b$) gives an expression to calculate electric currents once $\boldsymbol{b}$ is determined. This equation also guarantees that the electric current density is

https://doi.org/10.1017/S0022112006008810 Published online by Cambridge University Press

divergence-free, $\nabla \cdot \boldsymbol{j} = 0$. Further, the applied magnetic field must satisfy the magnetostatic equations, namely,

$$\nabla \cdot \boldsymbol{B}^0 = 0, \qquad \nabla \times \boldsymbol{B}^0 = 0, \tag{2.9}$$

which assure the solenoidal and irrotational character of $\boldsymbol{B}^0$.

### 2.1. *Applied magnetic field*

In order to simplify the numerical implementation, we assume that the applied magnetic field consists only of the dominant component in the normal direction, a common assumption in problems with non-uniform magnetic fields (Talmage & Walker 1988; Sterl 1990; Lavrent'ev *et al.* 1990; Ting *et al.* 1993; Sellers & Walker 1999). In these studies, one-dimensional approximations of fringing fields have been found to give reasonable results in many MHD duct flows. In dimensional terms, on placing the coordinate system in the centre of a rectangular surface with side lengths $X_0 = 2a$ and $Y_0 = 2b$, the normal component of the field produced by a single magnetized surface lying on the plane $Z = Z_0$ is given by (McCaig 1977)

$$\begin{aligned}\mathscr{B}_z^0 = \gamma B_{max} \Bigg\{ & \tan^{-1}\left(\frac{(X+a)(Y+b)}{(Z-Z_0)[(X+a)^2+(Y+b)^2+(Z-Z_0)^2]^{1/2}}\right) \\ & + \tan^{-1}\left(\frac{(X-a)(Y-b)}{(Z-Z_0)[(X-a)^2+(Y-b)^2+(Z-Z_0)^2]^{1/2}}\right) \\ & - \tan^{-1}\left(\frac{(X+a)(Y-b)}{(Z-Z_0)[(X+a)^2+(Y-b)^2+(Z-Z_0)^2]^{1/2}}\right) \\ & - \tan^{-1}\left(\frac{(X-a)(Y+b)}{(Z-Z_0)[(X-a)^2+(Y+b)^2+(Z-Z_0)^2]^{1/2}}\right)\Bigg\}, \end{aligned} \tag{2.10}$$

where $\mathscr{B}_z^0$ stands for the dimensional applied magnetic field and $\gamma$ is a normalization constant. Actually, (2.10) gives the normal component of the magnetic field generated by a finite size dipole and is a good approximation of a fringing magnetic field. For the sake of simplicity, we consider that the magnetized surface has a square shape, that is, $2a = 2b = L$. Therefore, $L$ is taken as the geometrical length scale used to non-dimensionalize the flow variables. We consider the superposition of two such parallel surfaces of the same size but with opposing polarization axes separated by a distance $2h$ and embedded on the bottom and top walls. Therefore, surfaces are located at $Z = -h$ and $Z = h$.

We also assume that the applied magnetic field is an independent function of the $z$-coordinate. If fact, the variation of the applied field in the normal direction is slight since the separation between the walls is small compared to the length of the flow domain in the $x$- and $y$-directions (see § 4.4). This variation is noticeable only very close to the top and bottom magnetized surfaces. Therefore, in the bulk of the flow the $z$-dependence can be neglected. Figure 1($b$) shows the dimensionless distribution of the normal component of the field in the bulk of the flow obtained by the superposition of two magnetized surfaces. The normalization constant $\gamma$ in (2.10) has been set in such a way that the maximum field strength in the central region is equal to 1. $B_z^0$ displays a rapid decay as the distance from the centre grows: it decays to 0.6 at the edge of the magnetized surfaces and to 0.03 when the distance from their centre is twice the side length of the square surfaces. Notice that border effects due to the square shape of the magnetized surfaces are smoothed out in the bulk.

While the three-dimensional expression of the field produced by the magnetized surfaces satisfies exactly the magnetostatic equations (2.9), if only the normal component

https://doi.org/10.1017/S0022112006008810 Published online by Cambridge University Press

is kept the field is no longer curl-free. However, retaining only this component is consistent with its dominant role in determining the flow dynamics. In fact, the magnetic field components in the $x$- and $y$-directions are very weak compared to the normal component and their influence on the flow is small. The magnetic field distributions considered here provide a good picture of the fringing effect and lead to reasonable results.

### 2.2. *Quasi-two-dimensional approximation*

In principle, the flow past a magnetic obstacle has a three-dimensional behaviour, mostly related to the existence of boundary layers at the solid boundaries. In fact, two different kinds of bounday layers are present, namely Hartmann layers within the magnetic obstacle zone and classic viscous boundary layers in the domain where the magnetic field is negligible. Therefore, generally speaking, a three-dimensional flow solution should be implemented. In the past, only a few time-dependent three-dimensional MHD computations have been performed over a finite-size domain (e.g. Mutschke *et al.* 1997; Mück *et al.* 2000). The flow past a magnetic obstacle is, however, significantly different from those mentioned above, since in both $x$- and $y$-directions the flow is unbounded. This requires boundary conditions to be formulated at infinity (for details on implementation of the boundary conditions see also § 4.1). The extension of the integration domain to infinity along with limitations on the integration time step due to stability considerations, make the three-dimensional computations for this case extremely costly. Based on our estimations, such computations are not feasible even if parallel computations are used. Fortunately, a simplified quasi-two-dimensional approach that retains the most important features of the flow can be applied. In fact, quasi-two-dimensionalization of flows occurs in a number of special cases, which are described very well in the literature. In addition to the suppresson of wall-normal motions by the action of a strong magnetic field (Sommeria & Moreau 1982) a few analogous mechanisms exist. For example, the force of gravity in a stratified flow (Voropayev, Afanasyev & Filippov 1991), the Coriolis force in a rotating homogeneous fluid (Zavala Sansón, van Heijst & Backx 2001) or the surface tension in a soap film (Couder & Basdevant 1986) tend also to two-dimensionilize the flow. Quasi-two-dimensional flows are also possible when a significant geometrical confinement is imposed, as in motions generated in shallow fluid layers. With a quasi-two-dimensional approach, the problem is usually formulated in terms of core variables, but the effect of the boundary layers is still included through an additional term in the momentum equation accounting for the wall friction.

We now justify the applicability of the quasi-two-dimensional approach to the reference case and specify particular conditions when three-dimensional effects can be neglected. With this aim, we consider two separate flow regions, namely the magnetic obstacle zone and the exterior zone, where the applied magnetic field is negligible. In the magnetic obstacle zone, the characteristic length scale in the $(x, y)$-plane is given by the size of the magnetized plates. Here, perturbations in the normal direction tend to be inhibited by the action of the strong magnetic field and a quasi-two-dimensional flow is promoted. The same mechanism is responsible for two-dimensionalization in MHD channel flows under strong magnetic fields. In the analysis of this kind of flow it is usual to split the flow domain into core and boundary layer regions (e.g. Müller & Bühler 2001). The most common boundary layers are the Hartmann layers formed at walls normal to the applied magnetic field. In a strong transverse magnetic field, the Hartmann layers are very thin ($O(Ha^{-1})$) and the core flow variables present a very slight variation along the magnetic field lines. Under these conditions it is reasonable

https://doi.org/10.1017/S0022112006008810 Published online by Cambridge University Press

to reduce the computational effort of solving a three-dimensional problem to a two-dimensional flow formulation for the core variables. Such an approach, originally established by Sommeria & Moreau (1982) in the context of turbulent flows in insulating wall ducts, has been successfully applied to a number of MHD channel flows by integration (averaging) of the equations along the magnetic field lines (e.g. Bühler 1996; Smolentsev 1997). In these cases, a uniform magnetic field extends over the whole flow region and the resulting quasi-two-dimensional flow retains the three-dimensional MHD effects through the Hartmann friction and a forcing term. The averaging procedure has also been applied to MHD flows under non-uniform magnetic fields. This was done by the first time in Lavrent'ev *et al.* (1990) where a steady channel flow of an electrically conducting fluid under a strong non-uniform field that varied along the duct axis was analysed. Three-dimensional effects due to the presence of Hartmann layers were introduced through a local Hartmann velocity profile along the magnetic field direction. This assumption was justified by both experimental (Bocheninskii *et al.* 1971) and theoretical (Kalyutik, Lavrent'ev & Serebryakov 1986) studies that demonstrated that even with low Hartmann numbers and interaction parameters the longitudinal velocity approached a local Hartmann profile. In addition, the effect of axial currents was introduced by solving the equation for the electric potential.

In the exterior zone, where the magnetic field does not directly affect the flow, three-dimensional perturbations are inhibited by the geometrical confinement. Here, the relevant length scale in the $(x, y)$-plane is given by the size of the vortical structures which are formed in the wake past the magnetic obstacle. In fact, this length scale is much larger than the characteristic dimension of the magnetic obstacle since the vortices tend to expand while proceeding downstream, as shown below. The conditions of the geometrical confinement that assure quasi-two-dimensionality are therefore easy to satisfy, provided that the distance between the solid boundaries is comparable with the size of the magnetic obstacle. Under these conditions, the same averaging procedure can be applied, leading to quasi-two-dimensional equations for the core variables. This is, for instance, the approach followed by Satijn *et al.* (2001) and Clercx, van Heijst & Zoeteweij (2003) in modelling shallow water flows where the bottom friction is parameterized through an additional linear term often referred as Rayleigh friction. It should be noted that the core variables obtained by integrating the equations over the magnetic obstacle zone coincide with the real distributions in the core, while the core variables within the exterior region just represent the result of integration. From this point of view, the averaging approach is more accurate when it is applied to the magnetic obstacle zone.

Following the quasi-two-dimensional approach, we assume that the transport of momentum in the normal direction is mainly diffusive so that the velocity components can be expressed in the form

$$u(x, y, z, t) = \overline{u}(x, y, t) f(x, y, z), \qquad v(x, y, z, t) = \overline{v}(x, y, t) f(x, y, z), \tag{2.11}$$

where $\overline{u}$ and $\overline{v}$ are the velocity components in the $x$- and $y$-directions, respectively, averaged in the normal direction (core variables), and the function $f$ accounts for the variation of the velocity profile in this direction. Its dependence on the $x$- and $y$-coordinates must reflect the different flow regions due to the localization of the magnetic field. The function $f$ must satisfy non-slip conditions at the walls, as well as the symmetry condition $\partial f/\partial z = 0$ at the mid-plane. In addition, $f$ must also satisfy the normalization condition, namely $\int_0^\alpha U f \, \mathrm{d}z = \alpha$, where $\alpha = h/\mathscr{L}$ is the aspect ratio, $\mathscr{L}$ being the relevant length scale of the flow in the $(x, y)$-plane. The form (2.11) is a strong assumption but is a reasonable approximation when the magnetic field is

https://doi.org/10.1017/S0022112006008810 Published online by Cambridge University Press

strong or when $h \ll \mathscr{L}$. As already mentioned, the scale $\mathscr{L}$ is different for the two flow regions.

Similarly to Lavrent'ev *et al.* (1990), we assume that the normal variation of the velocity components is given by the function $f$ as follows:

$$f = \frac{\alpha \mathscr{H}a}{\alpha \mathscr{H}a - \tanh(\mathscr{H}a\alpha)} \left(1 - \frac{\cosh(\mathscr{H}az)}{\cosh(\mathscr{H}a\alpha)}\right), \tag{2.12}$$

where the local Hartmann number is defined as $\mathscr{H}a(x, y) = HaB_z^0(x, y)$. If equations (2.11) and (2.12) are substituted in (2.1) and (2.2) and integrated in the $z$-coordinate from 0 to $\alpha$, taking into account that walls are electrically insulated, a two-dimensional system of equations is obtained:

$$\frac{\partial u}{\partial x} + \frac{\partial v}{\partial y} = 0, \tag{2.13}$$

$$\frac{\partial u}{\partial t} + u\frac{\partial u}{\partial x} + v\frac{\partial u}{\partial y} = -\frac{\partial p}{\partial x} + \frac{1}{Re}\nabla_\perp^2 u - \frac{u}{\tau} + \frac{Ha^2}{Re} j_y B_z^0, \tag{2.14}$$

$$\frac{\partial v}{\partial t} + u\frac{\partial v}{\partial x} + v\frac{\partial v}{\partial y} = -\frac{\partial p}{\partial y} + \frac{1}{Re}\nabla_\perp^2 v - \frac{v}{\tau} - \frac{Ha^2}{Re} j_x B_z^0, \tag{2.15}$$

where the overline in the velocity components has been dropped and the subindex $\perp$ denotes the projection of the $\nabla$ operator on the $(x, y)$-plane. In addition to viscous dissipation effects in this plane, represented by the second term on the right-hand side of equations (2.14) and (2.15), terms taking into account the Hartmann–Rayleigh friction are also present. These involve a characteristic time scale, $\tau$, for the decay of vorticity due to dissipation in the Hartmann and viscous layers. The inverse of this timescale is given by

$$\tau^{-1} = \frac{1}{\alpha Re}\frac{\partial f}{\partial z}\bigg|_0^\alpha = \frac{\mathscr{H}a^2}{Re}\frac{\sinh(\alpha\mathscr{H}a)}{\alpha\mathscr{H}a\cosh(\alpha\mathscr{H}a) - \sinh(\alpha\mathscr{H}a)}. \tag{2.16}$$

Notice that for $\mathscr{H}a \gg 1$, equation (2.16) reduces to the usual form of the Hartmann braking coefficient, namely, $\tau^{-1} = \mathscr{H}a/\alpha Re$. In fact, $\tau$ is the ratio of a typical eddy turnover time $\mathscr{L}/U$ and a typical time scale for the Hartmann braking, $(h/B_{max})(\rho/\sigma\nu)^{1/2}$. In turn, if $\mathscr{H}a \to 0$ (which occurs outside the obstacle region) it can be shown from a Taylor's expansion that the coefficient becomes $\tau^{-1} = \lambda\mathscr{L}/U$ where $\lambda = 3\nu/2h^2$ is the inverse of a viscous diffusion time. This limit corresponds to the viscous friction in the Hele–Shaw approximation (Bühler 1996).

Equations (2.13)–(2.15) retain the time dependence associated with inertial effects. Under this approximation the flow dynamics is determined by the interaction of the normal component of the applied field with current loops in planes parallel to the walls as well as by the Hartmann–Rayleigh friction in the boundary layers. However, we will consider conditions where inertial effects dominate over Hartmann–Rayleigh friction, namely conditions where the time scales for Hartmann braking and viscous diffusion are much larger than the eddy turnover time. In fact, since we are assuming that confining walls are insulating, the damping due to Hartmann braking near the obstacle region is weaker than, for instance, with conducting walls (Bühler 1996). Several numerical tests have shown that for the flow regimes analysed in the present study, the dominance of inertial effects over Hartmann braking in the magnetic obstacle region is assured provided that $h/L = 2$. Under these conditions, it is also assured that outside the obstacle the viscous diffusion time is much larger than the eddy turnover time. In fact, this condition is expressed through the inequality

https://doi.org/10.1017/S0022112006008810 Published online by Cambridge University Press

$2\alpha^2 Re(L/3\mathscr{L}) \gg 1$, which is satisfied for the Reynolds numbers explored (100 and 200) since the length scale of the flow outside the obstacle, $\mathscr{L}$, is about an order of magnitude larger than the length of the magnetized plates $L$ (see § 5). In this way, the confinement condition $h \ll \mathscr{L}$ is also satisfied.

In the quasi-two-dimensional approximation the induction equation (2.7) reduces to a single equation for the component $b_z$:

$$\nabla_\perp^2 b_z - u\frac{\partial B_z^0}{\partial x} - v\frac{\partial B_z^0}{\partial y} = 0. \tag{2.17}$$

From Ampere's law (2.8*b*), the current density components in the bulk are given by

$$j_x = \frac{\partial b_z}{\partial y}, \qquad j_y = -\frac{\partial b_z}{\partial x}. \tag{2.18}$$

Equations (2.18) show that the induced magnetic field serves as a stream function for the electric current density. Therefore, lines of $b_z = \text{const.}$ are current streamlines.

Ultimately, the quasi-two-dimensional flow approximation can only be validated by comparison with three-dimensional calculations and experimental measurements. The experimental studies by Honji (1991) and Honji & Haraguchi (1995) in a thin layer of an electrolytic solution seem to indicate that a reasonable simulation of this kind of phenomenon can be achieved with a quasi-two-dimensional approach.

Finally, boundary conditions must be established for the core velocity and induced magnetic field. We assume that far away from the magnetic obstacle, a steady uniform flow in the positive $x$-direction is imposed. With the origin of coordinates located at the point of maximum magnetic field strength, the boundary conditions for the velocity components are

$$u \to 1 \qquad v \to 0, \qquad \text{as } x, y\pm \to \infty. \tag{2.19}$$

It is expected that the strength of the induced magnetic field is higher near the zone where the applied field is strong. As the distance from the source of the applied field grows, the induced field must decrease and vanish at infinity. Therefore, it must satisfy

$$b_z \to 0 \quad \text{as } x, y \to \pm\infty. \tag{2.20}$$

In § 4.1 these conditions are adapted for the numerical implementation. In figure 1(*c*), the geometrical parameters and the configuration of the quasi-two-dimensional core flow are shown. The centre of the magnetic obstacle, that is, the point of maximum magnetic field strength, is located at a distance $X_u$ from the inlet and a distance $X_d$ from the outlet. $X_u$ and $X_d$ are measured in units of the characteristic length $L$. $H$ is the separation between the lateral boundaries which determines the solid blockage of the confined flow characterized by the blockage parameter, $\beta = 1/H$. It can be observed that the applied magnetic field isolines form concentric circles inside and outside the region covered by the magnetized plates.

## 3. Preliminary description of the flow

We offer here an introductory qualitative description of the phenomena involved in the flow past a magnetic obstacle. This flow has some resemblance with the duct flow at the entrance/exit of a magnet (Müller & Bühler 2001; Moreau 1990), though the size of the obstacle and the absence of lateral (side) walls change the flow structure strongly. The fluid passing through the magnetic obstacle encounters mainly four different regions of fringing magnetic field. The lateral fringing regions have a

https://doi.org/10.1017/S0022112006008810 Published online by Cambridge University Press

secondary effect on the flow in most cases while inlet and outlet fringing regions are always of primary importance. In a short distance (on the order of the characteristic length of the obstacle), the oncoming fluid passes from a region of nearly zero magnetic field to one with $O(1)$ strength, and then again to a region of negligible field. Different flow regimes can be observed depending on the values of the Reynolds and Hartmann numbers. For the Reynolds numbers explored in this study, stationary as well as periodic solutions were found depending on the value of $Ha$.

In the neighbourhood of the inlet fringing zone the oncoming fluid passes from a region of low-intensity field to one with a high intensity. The electromotive force $\boldsymbol{u} \times \boldsymbol{B}^0$ induces a lower voltage in the low-intensity region and a higher voltage in the region where the field is stronger. The voltage difference drives a current in the flow direction for $y > 0$ and in the opposite direction for $y < 0$. These currents close in the cross-stream direction upstream and downstream of the inlet fringing zone. When the fluid moves through the outlet fringing zone, the voltage difference is inverted, as is the current circulation. Therefore, upstream of the obstacle, currents circulate clockwise and produce an induced magnetic field in the normal direction that points downwards, in accordance with Lenz's law. Downstream of the obstacle, the current circulation is anti-clockwise and the induced magnetic field points upwards. Under certain conditions, only these two main current loops are formed. However, additional current loops may appear. The number and particular structure of current loops depend on both Reynolds and Hartmann numbers, as will be shown by the numerical results.

In the duct flow at the entrance or exit of a magnet, the sidewalls confine the current loops in such a way that they are elongated in the flow direction, intensifying the streamwise current density components. This is of particular importance when the sidewalls are electrically insulated. The current density components in the streamwise direction give rise to Lorentz forces that point towards the sidewalls. This provokes the expulsion of the volumetric flow from the core towards the side layers with high velocities and, therefore, an M-shape velocity profile is created (Müller & Bühler 2001; Moreau 1990). In contrast, in the flow past a magnetic obstacle where sidewalls are absent, current loops tend to spread in the flow domain. In the region of high-intensity field, currents close through the lateral fringing zones and, consequently, cross-stream current density components are dominant. In fact, in this region electric currents from the upstream and downstream loops reinforce flowing in the negative direction, transverse to the main flow. The current density interacts with the magnetic obstacle field giving rise to a non-uniform Lorentz force that points mainly in the streamwise direction, opposing the flow and creating vorticity. This causes a pressure increase in the neighbourhood upstream of the obstacle, while downstream it drops abruptly. For $Re = 100$ and a small Hartmann number ($Ha \approx 1$–$10$), the fluid moves with reduced velocity through the high-intensity field region. As the Hartmann number increases and the opposing Lorentz force is stronger, the oncoming fluid tends to flow around the obstacle and a noticeable cross-stream velocity component appears. Figure 2 shows streamtracers for $Re = 100$ with two different Hartmann numbers ($Ha = 20$ and 30). It can be seen that the flow past a magnetic obstacle displays some of the characteristic regions observed in the flow around a cylinder, namely a region of retarded flow upstream of the obstacle, two sidewise regions of displaced and accelerated flow, and a wake downstream of the obstacle (Zdrakovich 1997; Oertel 1990). In the neighbourhood of the lateral fringing zones, the velocity is higher than near the central region where the opposing force is more intense. This leads to a velocity deficit in the central region, and the creation of two lateral free-shear layers parallel and aligned with the main flow direction where a maximum and a minimum of

https://doi.org/10.1017/S0022112006008810 Published online by Cambridge University Press

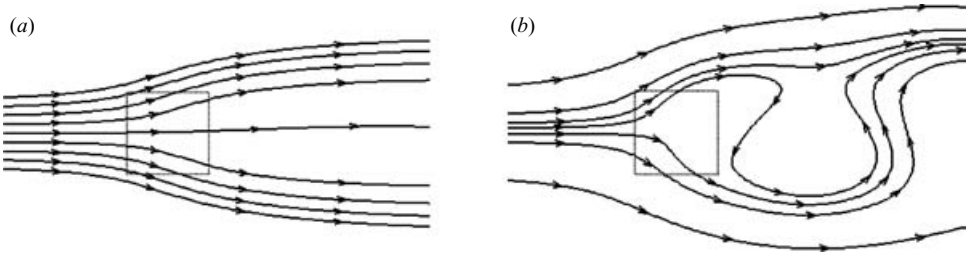



FIGURE 2. Streamtracers in the flow past a magnetic obstacle for $Re = 100$. (*a*) $Ha = 20$; (*b*) $Ha = 30$. The applied field comes out of the plane of flow. The dotted square denotes the area covered by the magnetized surfaces.

vorticity exist. When the Hartmann number is about 20 (figure 2*a*) the fluid may become stagnant in the region of intense field, while far away from the obstacle the flow remains nearly unperturbed. If the Hartmann number is sufficiently high ($Ha \approx 22$), vortices can appear in the near wake. These vortices, although created by Lorentz forces, are formed and evolve inside a negligible magnetic field. When convective effects and the magnetic braking are strong enough, the wake can become destabilized and present unsteady behaviour (figure 2*b*). In fact, a periodic vortex shedding similar to the von Kármán street in the flow around a cylinder, can be observed. In § 5 a detailed analysis of the flow structure will be carried out for the restricted values of Reynolds and Hartmann numbers considered in this study. In the following section we present the numerical methods used in this work.

## 4. Numerical methods

A numerical simulation approach has been taken to treat the problem of the flow past a magnetic obstacle. In this section, we summarize the numerical methods and the tests carried out to evaluate the numerical performance.

### 4.1. *Boundary conditions*

The main flow was assumed to be in the $x$-direction and, at the inlet, a uniform flow was prescribed:

$$u = 1, \qquad v = 0. \tag{4.1}$$

In numerical studies involving vortex shedding, the formulation of outflow boundary conditions deserves special attention in order to avoid numerical inaccuracies. The most common boundary conditions studied in the literature of flows around cylinders are Neumann and convective boundary conditions. Several numerical analyses have been carried out to determine the performance of these conditions in different flow situations (Zdravkovich 1997; Bruneau & Fabrie 1994; Sohankar, Norberg & Davidson 1998, 1999). Although convective boundary conditions have shown the possibility of reducing the distance from the obstacle to the outlet without affecting the global flow pattern, Neumann conditions perform well provided that the downstream distance $X_d$ is sufficiently large. In this work, Neumann boundary conditions

$$\frac{\partial u}{\partial x} = \frac{\partial v}{\partial x} = 0 \tag{4.2}$$

https://doi.org/10.1017/S0022112006008810 Published online by Cambridge University Press

were applied at the outlet. At the lateral boundaries, symmetry-type conditions simulating a frictionless wall were imposed:

$$\frac{\partial u}{\partial y} = v = 0. \tag{4.3}$$

Finally, we assume that the induced field is zero at a long enough finite distance from the source of the applied field. Therefore, we impose that the single component of the induced field satisfies the condition

$$b_z \mid_S = 0, \tag{4.4}$$

where the subindex $S$ denotes the boundaries of the integration domain.

### 4.2. *Numerical solution*

The numerical solution was addressed using a formulation based on the primitive variables, the velocity and pressure, and the induced magnetic field as electromagnetic variable. A finite difference method on an orthogonal equidistant grid was used to solve the governing equations (2.13)–(2.15) and (2.17) under boundary conditions (4.1)–(4.4), assuming a motionless fluid as initial condition. A spatial discretization of second-order accuracy was done on a staggered grid arrangement while the Euler method was used for time discretization. Accurate time integration was provided by choosing a small enough time step (see § 4.4). The velocity components $u$ and $v$ were defined at the midpoints of the vertical and horizontal surfaces of the computational cell, respectively, while the pressure and the induced magnetic field were defined at the centre of the cell. Diffusive terms were discretized using central differences. For convective terms a mixture of central differences and the donor-cell discretization, as suggested in Hirt, Nichols & Romero (1975), was implemented. For the solution of the governing equations, the standard time-marching procedure described in Griebel, Dornseifer & Neunhoeffer (1998) was extended to consider MHD flows. The time discretization of the momentum equations was explicit in the velocities and implicit in the pressure:

$$u^{(n+1)} = F^{(n)} - \delta t \frac{\partial p^{(n+1)}}{\partial x}, \qquad v^{(n+1)} = G^{(n)} - \delta t \frac{\partial p^{(n+1)}}{\partial y},$$

where

$$F^{(n)} = u^{(n)} + \delta t \left[ \frac{1}{Re} \left( \frac{\partial^2 u}{\partial x^2} + \frac{\partial^2 u}{\partial y^2} \right) - \frac{\partial (u^2)}{\partial x} - \frac{\partial (uv)}{\partial y} - \frac{u}{\tau} + \frac{Ha}{Re} j_y B_z^0 \right],$$

$$G^{(n)} = v^{(n)} + \delta t \left[ \frac{1}{Re} \left( \frac{\partial^2 v}{\partial x^2} + \frac{\partial^2 v}{\partial y^2} \right) - \frac{\partial (uv)}{\partial x} - \frac{\partial (v^2)}{\partial y} - \frac{v}{\tau} - \frac{Ha}{Re} j_x B_z^0 \right].$$

The continuity equation was satisfied by solving a Poisson equation for the pressure $p^{(n+1)}$ at time $t_{n+1}$. This algorithm corresponds to the Chorin projection method (Chorin 1968). The Poisson equation was solved subject to homogeneous Neumann conditions on the boundary, simulating far-field conditions commonly used in the analysis of flows past solid obstacles in unbounded regions. The Gauss–Seidel method was used for the solution of the pressure Poisson equation, which was iterated until the divergence of the velocity field reached values of the order of $10^{-5}$. Equation (2.17) for the induced magnetic field $b_z$ was solved at $t_{n+1}$ using the same method. Electric current density components were calculated through (2.18), for which the divergence-free condition is satisfied based on the vector identity $\nabla \cdot (\nabla \times \boldsymbol{b}) = 0$.

https://doi.org/10.1017/S0022112006008810 Published online by Cambridge University Press

### 4.3. *Global flow coefficients*

In order to characterize the performance of the numerical scheme under different conditions, the behaviour of two global flow coefficients was analysed. Due to the similarities with the flow around bluff bodies, we used the base pressure coefficient and the Strouhal number to characterize the flow. The hydrodynamic base pressure coefficient is defined as (Blackburn & Henderson 1999)

$$C_{pb} = 1 + \frac{p_{180} - p_0}{p_d}, \tag{4.5}$$

where $p_0$ and $p_{180}$ are the pressures at the furthest upstream and downstream points on the body surface, and $p_d$ is the free-stream dynamic pressure $\rho U^2/2$. Since in our problem there is no solid obstacle, we consider $p_0$ and $p_{180}$ to be the pressures on the axial midline at the furthest upstream and downstream points, respectively, on the perimeter of the projection of the magnetized surfaces on the plane of motion. We found that $C_{pb}$ or its negative (known as the base suction coefficient), are suitable quantities for the description of the present problem. In fact, it has been found that, in the flow around bluff bodies, these coefficients respond sensitively to the changes in the flow instabilities in different flow regimes (Williamson 1996).

The Strouhal number is commonly used to characterize vortex shedding phenomena and is defined as

$$St = \frac{fL}{U} \tag{4.6}$$

where here $f$ is the shedding frequency. In this study, the Strouhal number was determined from the fluctuating values of vorticity in the wake behind the obstacle.

### 4.4. *Numerical grid resolution, time step and obstacle location*

In the numerical simulation of hydrodynamic flows around bluff bodies it is common to use non-uniform grids that allow a finer resolution near the solid body and a coarser one in the wake behind it (e.g. Sohankar *et al.* 1998, 1999; Blackburn & Henderson 1999). An accurate resolution of boundary layers on the solid body is a requirement for an adequate description of the flow. However, a uniform grid has been used to deal with the flow around a square cylinder under a uniform magnetic field (Mück *et al.* 2000). These authors claim that a non-uniform grid seems not to be appropriate because numerical diffusion may dominate over the MHD damping. In the present problem, the use of an orthogonal equidistant grid appears to also be the most convenient choice. Since no solid body exists in the integration region, there are no thin boundary layers to resolve. However, a sufficiently fine grid is needed to resolve the shear layers that are formed in the neighbourhood of the magnetic obstacle and in the flow wake.

In this work, two different Reynolds numbers were explored, namely 100 and 200. In both cases the Hartmann number varied in the range $1 \leqslant Ha \leqslant 100$. Under these conditions, numerical experiments have shown the appearance of flow structures with different typical sizes. The smaller ones are comparable with the length of the magnetized surfaces in the neighbourhood of the magnetic obstacle, but much larger structures are also formed in the wake. These structures were also observed in the experiments by Honji & Haraguchi (1995). Therefore, a suitable grid must be able to fully resolve this kind of structure. The blockage parameter in the flow configuration used in the present study was fixed at 5 % and the length of the flow domain was varied according to the Reynolds number. This length was either 35 or 50 units for $Re = 100$, and 35 for $Re = 200$. Several numerical tests indicated that reasonable results can be obtained with a minimum of 8 points in the cross-stream direction and 4–5 points

https://doi.org/10.1017/S0022112006008810 Published online by Cambridge University Press

in the streamwise direction per unit area. For $Re = 100$, most of the computations were performed using constant cell sizes of $\Delta_x = 0.21$ and $\Delta_y = 0.1$ with a grid size $211 \times 201$. The grid convergence was checked through numerical tests using $\Delta_x = 0.1$, $\Delta_y = 0.06$ (10 and 16 nodes in the streamwise and cross-stream directions, with a grid size $351 \times 341$) and $\Delta_x = 0.4$, $\Delta_y = 0.2$ (2.5 and 5 nodes in the streamwise and cross-stream directions with a grid size $101 \times 101$). It was found that the flow is well-resolved with cell sizes $\Delta_x = 0.21$ and $\Delta_y = 0.1$: results showed a difference of less than 3 % in the base pressure coefficient and the Strouhal number for the case $\Delta_x = 0.1$, $\Delta_y = 0.06$. For $Re = 200$, smaller cell sizes were used, $\Delta_x = 0.15$ and $\Delta_y = 0.09$, with the grid size $233 \times 221$, and grid convergence was also verified. From numerical calculations of two-dimensional flows around cylinders Sohankar *et al.* (1998) recommend that for the range $Re \leqslant 200$ the cell Reynolds number, based on $\Delta_x$, should be less than 30. This is indeed the case for all flows treated in this work.

We initiated the time-marching calculations with the fluid at rest. The effects of the integration time step on the global flow behaviour were also evaluated. For $Re = 100$, negligible variations of less than 1 % were detected in the Strouhal number when the time step changed from 0.005 to 0.0025. The same variation in $\Delta t$ yields a difference of less than 2 % in the base pressure coefficient. Therefore, the value $\Delta t = 0.005$ was considered to be small enough to guarantee accurate computations.

Several numerical tests were performed to determine a suitable location of the magnetic obstacle. The base pressure coefficient and the Strouhal number were used to evaluate changes in the global flow pattern due to the obstacle location, so that inlet effects as well as upstream effects from the outlet can be minimized. For both $Re = 100$ and 200, it was determined that an upstream distance $X_u = 10$ and a minimum downstream distance $X_d = 25$ guarantee results that are nearly independent of the location of the obstacle. Similar results were found by Sohankar *et al.* (1998) at moderate Reynolds numbers ($45 \leqslant Re \leqslant 200$) using free-stream conditions, equation (4.1), and Neumann outflow conditions, equation (4.2).

Evidently, $X_u$, $X_d$ and $H$ are relevant not only because of the hydrodynamic effects, but also because of magnetohydrodynamic considerations. In fact, these distances have to be long enough to allow the induced magnetic field to approach zero at the boundaries. Incidentally, the induced field decays very fast: in the range of Hartmann numbers explored in this work it varies from values of the order $10^{-2}$ near the zone of maximum applied magnetic field strength to $10^{-4}$ within a distance of 10 units in the streamwise direction, and to $10^{-6}$ within the same distance in the cross-stream direction. Therefore, geometrical factors are mainly determined in compliance with hydrodynamic requirements.

## 5. Numerical results

We now present the numerical results for the two Reynolds numbers explored, 100 and 200, in the range of Hartmann numbers $1 \leqslant Ha \leqslant 100$. Under these conditions, the laminar flow may display either steady or time-dependent solutions. For each Reynolds number, three different laminar flow regimes were detected according to the value of the Hartmann number: steady, transition and periodic vortex shedding. In what follows, we present a description of these regimes for $Re = 100$ and $1 \leqslant Ha \leqslant 100$. Afterwards, we discuss the variations found as the Reynolds number grows.

### 5.1. *Steady flow*

For $Re = 100$, this regime appears in the range $1 \leqslant Ha < 20$. Once the transient state finishes, the flow shows a stable time-independent behaviour characterized by the

https://doi.org/10.1017/S0022112006008810 Published online by Cambridge University Press

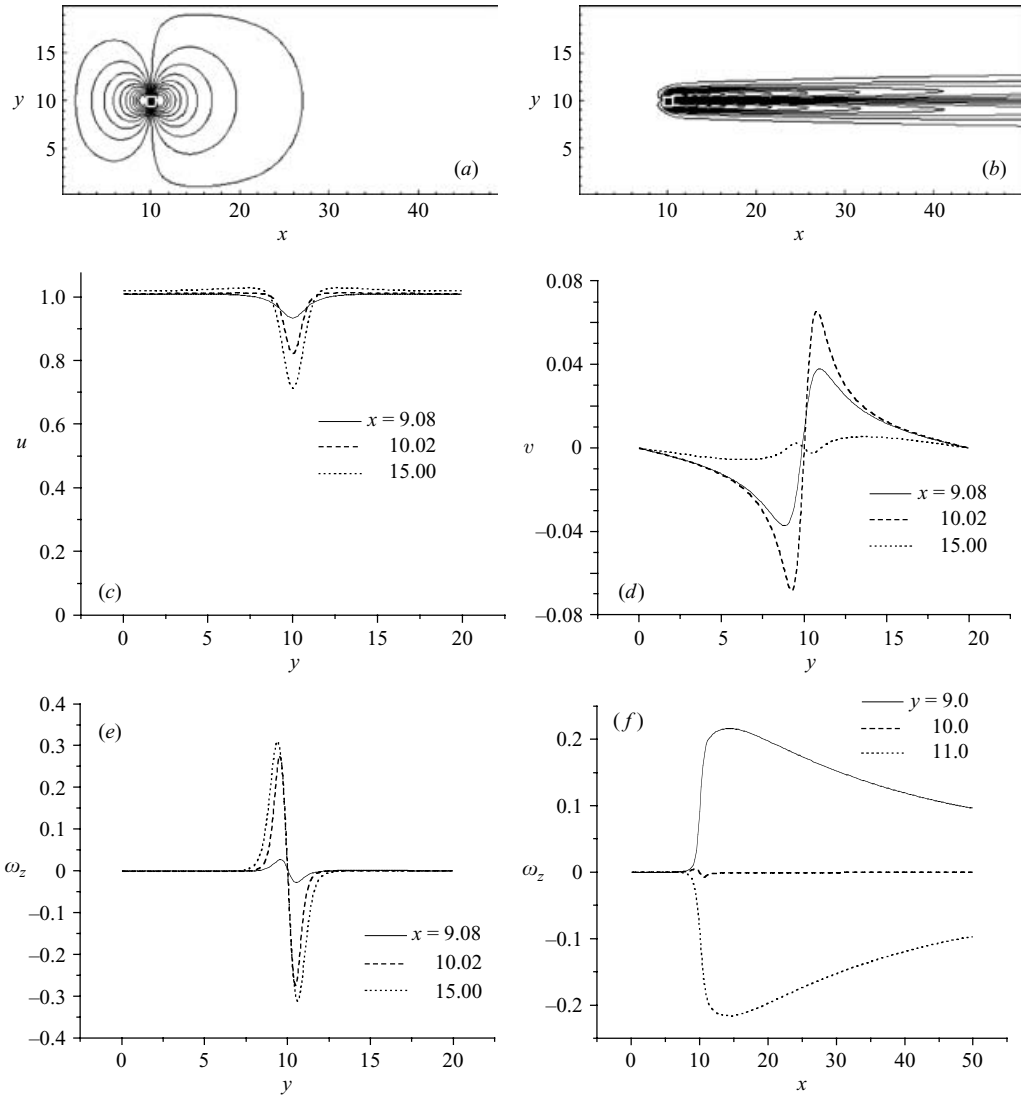



FIGURE 3. (*a*) Induced magnetic field isolines. (*b*) Vorticity isolines. (*c*) Streamwise velocity component and (*d*) cross-stream velocity component vs. cross-stream coordinate. (*e*) Vorticity vs. cross-stream coordinate. (*f*) Vorticity vs. streamwise coordinate. $Re = 100$, $Ha = 10$, $N = 1$.

formation of two loops of induced magnetic field up- and downstream of the obstacle and a long, low-velocity wake behind it. Figure 3(*a*, *b*) shows the induced magnetic field and vorticity isocontours for the case $Re = 100$, $Ha = 10$, that corresponds to $N = 1$. The projection of the magnetized surfaces on the plane of motion is shown through a unit square for visualization purposes. The induced field takes negative values upstream of the obstacle and smoothly changes to positive values as it goes downstream. Inside the obstacle, the current is distributed uniformly and points in the negative $y$-direction; therefore, the interaction with the magnetic field produces a Lorentz force that opposes the fluid motion. Consequently, the pressure rises upstream as the obstacle is approached and drops suddenly downstream in a distance on the order of the characteristic length. Symmetry with respect to the mid-horizontal axis

https://doi.org/10.1017/S0022112006008810 Published online by Cambridge University Press

can be observed; notice that the effect of convection is clearly shown not only for the vorticity but also for the induced magnetic field, whose isocontours are slightly elongated in the flow direction. The wake extends along the whole downstream integration region while its width of about 4 units remains approximately constant. In figure 3($c$–$f$) the velocity and vorticity profiles for the same Reynolds and Hartmann numbers are presented. They resemble the profiles found in the laminar flow around a cylinder for low Reynolds numbers (Zdrakovich 1997; Oertel 1990). The velocity deficit caused by the braking of the fluid in the obstacle region increases with the streamwise distance. The deficit is of about 5 % at a distance of 1 unit upstream of the obstacle centre (retarded flow region) and reaches about 30 % at a distance of 5 units downstream from that point (see figure 3$c$). The cross-stream velocity component is one order of magnitude smaller than the streamwise component, with its highest value at the obstacle centre (see figure 3$d$). The occurrence of a cross-stream velocity component in the obstacle region gives rise to a local shear flow that is more pronounced the higher the Hartmann number. However, no stagnation nor recirculating flow regions are observed. This is the main feature of the flow in this range of Hartmann numbers. Vorticity profiles in figures 3($e$) and 3($f$) display negative and positive regions, up and down the mid-horizontal axis, respectively. Notice that the vorticity magnitude at the end of the wake (40 units dowstream of the obstacle) remains at 50 % of its maximum value, which is taken about three units downstream of the obstacle centre.

### 5.2. *Transition flow*

For $Re = 100$, transition flow occurs in the range $20 \leqslant Ha \leqslant 25$. In this regime the flow develops a time-periodic behaviour characterized by the formation of elongated vortices in the near wake that are eventually shed. The periodic flow has been mainly characterized by analysing the time dependence of vorticity in the wake. Figure 4 shows the vorticity as a function of time at the axial midline at a position 15 units downstream of the centre of the obstacle, for different Hartmann numbers. For $Ha =$ 20 an incipient oscillation is detected, but it is damped out after nearly 75 dimensionless time units. The velocity field is very similar to those of the previous regime, presenting no recirculation nor stagnation regions. For $Ha = 21$ the oscillation is sustained longer and a very weak recirculation region is formed outside the magnetic obstacle, in what can be called the near wake. This region is composed of upper and lower vortices with clockwise and anticlockwise circulation, respectively. The vortices start forming 2 units downstream of the obstacle centre and have an approximate length of 2 units and a width of 0.5 each. Two stagnation points can be identified at the extremes of this region. The value $Ha = 21.5$ appears to be the threshold for sustained flow oscillations; it corresponds to an interaction parameter $N = 4.6$. As the Hartmann number is increased to 22, the vorticity oscillation is maintained with a small, variable amplitude. The flow field displays a wave-like motion along the wake. The recirculation is more intense and starts 1 unit from the centre of the obstacle, the length of the vortices growing to approximately 6 units, keeping the same width. For $Ha = 23$ vortex shedding arises and the vorticity at the mid-wake axis presents a uniform growth in amplitude until it reaches, after a transient time, a constant value. Figure 5 shows the velocity field and vorticity isolines at $t = 300$ for this Hartmann number. Analysis of instantaneous velocity fields reveals that vortices are no longer symmetically located one above the other, but are displaced (see figure 5$a$). Vortices travel a distance of about 7 units along the wake before complete damping, after which a wavy motion remains in the rest of the domain that can be identified as the

https://doi.org/10.1017/S0022112006008810 Published online by Cambridge University Press

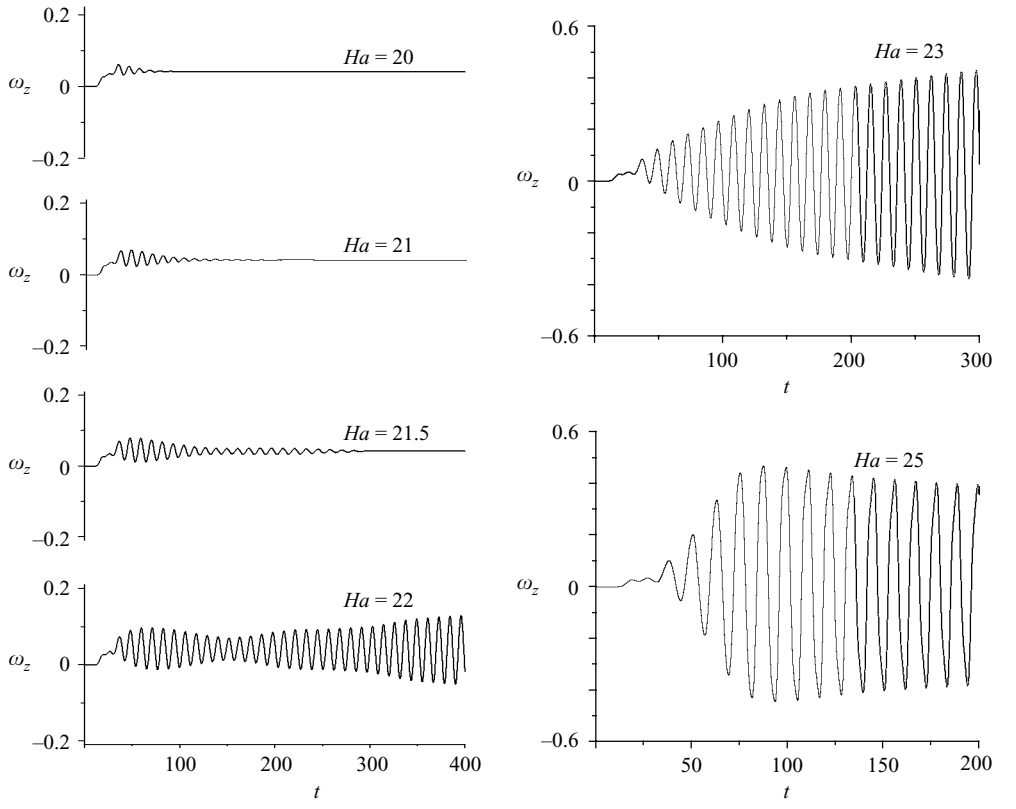



FIGURE 4. Vorticity as a function of time on the centreline at a distance of 15 units downstream the centre of the magnetic obstacle for different Hartmann numbers. $Re = 100$.

far wake (see figure 5*b*). For $Ha = 25$ the vortex shedding process is well-established and the vorticity reaches its constant amplitude in a reduced transient time.

### 5.3. *Periodic vortex shedding flow*

For $Re = 100$ the periodic vortex shedding appears in the range $25 < Ha \leqslant 100$. Figure 6 shows instantaneous vorticity isocontours for $Ha = 30$ ($N = 9$). This is taken as a reference value for the description of the time-periodic flow regime. The evolution of the wake can be observed from its incipient formation to the establishment of the periodic vortex shedding. Initially, the formation of shear layers at both sides of the obstacle is promoted. They remain parallel and aligned with the main flow direction, displaying a maximum and minimum of vorticity a few units downstream the obstacle centre. As the flow travels downstream, the shear layers become unstable. The onset of the instability is manifested by the appearance of a transverse oscillation on the mid-horizontal axis along the wake, presenting a wavelength of about 10 units, which remains approximately constant in time while the amplitude of the oscillation grows. The instability first appears far downstream from the magnetic obstacle, approximately 8 length units from its centre, where both the applied and induced magnetic fields are negligible. This means that the instability is related to the specific shape of the velocity profile, which is formed by the action of the magnetic field near the obstacle. As time proceeds, the wake develops in the cross-stream direction also and achieves a span of more than 10 units. A close resemblance with the wake formed

https://doi.org/10.1017/S0022112006008810 Published online by Cambridge University Press

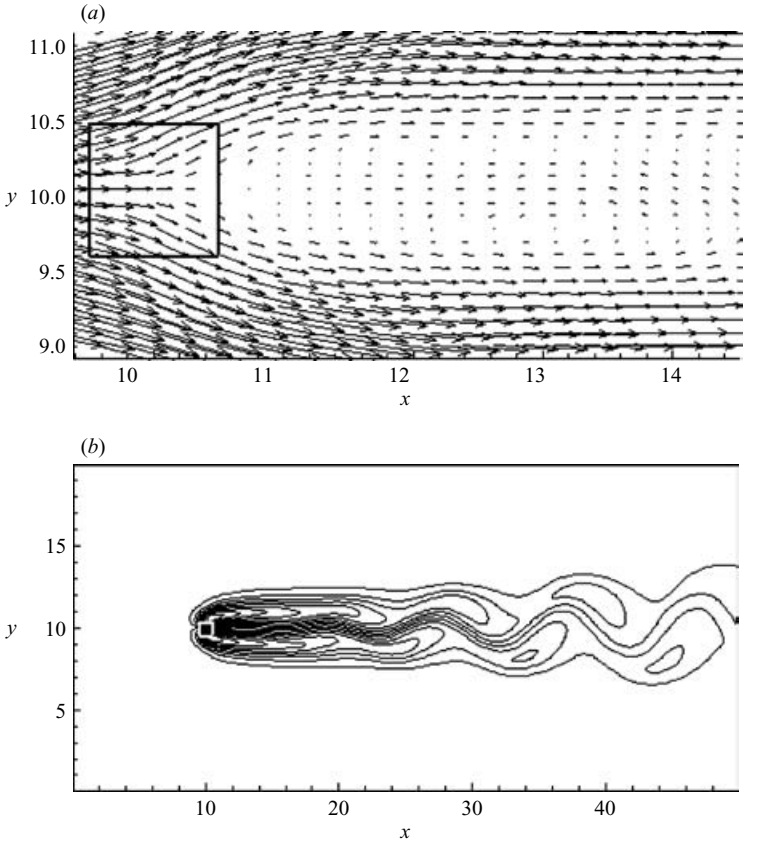



FIGURE 5. (*a*) Detailed view of the instantaneous velocity field in the near wake. (*b*) Instantaneous vorticity isolines. $t = 300$, $Ha = 23$.

behind a cylinder is observed. However, the flow around a cylinder becomes unstable due to intrincate mechanisms that involve adverse pressure gradients in the viscous boundary layers and interactions with the near wake. It is worth noting that in the magnetic obstacle flow, although the instability itself results from the velocity profile, it is not directly affected by the magnetic field. Therefore, as in the flow around a cylinder, in the present case the instability evolves in the absence of a magnetic field.

The plot of vorticity as a function of time is very similar to that corresponding to $Ha = 25$ (see figure 4). For $Ha = 30$ a transient time of about 100 time units elapses before the vortex shedding appears. The transient time is slightly reduced the higher the Hartmann number. The Strouhal number that characterizes the vortex shedding was close to 0.1, which differs from the values around 0.150 usually reported for the two-dimensional flow past a cylinder (e.g. Sohankar *et al.* 1998). The Strouhal number was calculated at downstream distances of 7.5 and 15 units from the obstacle centre, presenting variations of less than 1 %. Honji & Haraguchi (1995) found a Strouhal number of 0.1 in their experiments with a moving magnet in a thin layer of an electrolytic solution. However, the coincidence with the experimental value should be taken with caution, since important differences between the experiment and the present numerical calculations exist. In the experiment, the Hartmann number was close to 1, but an additional braking was introduced by injecting a direct current

https://doi.org/10.1017/S0022112006008810 Published online by Cambridge University Press

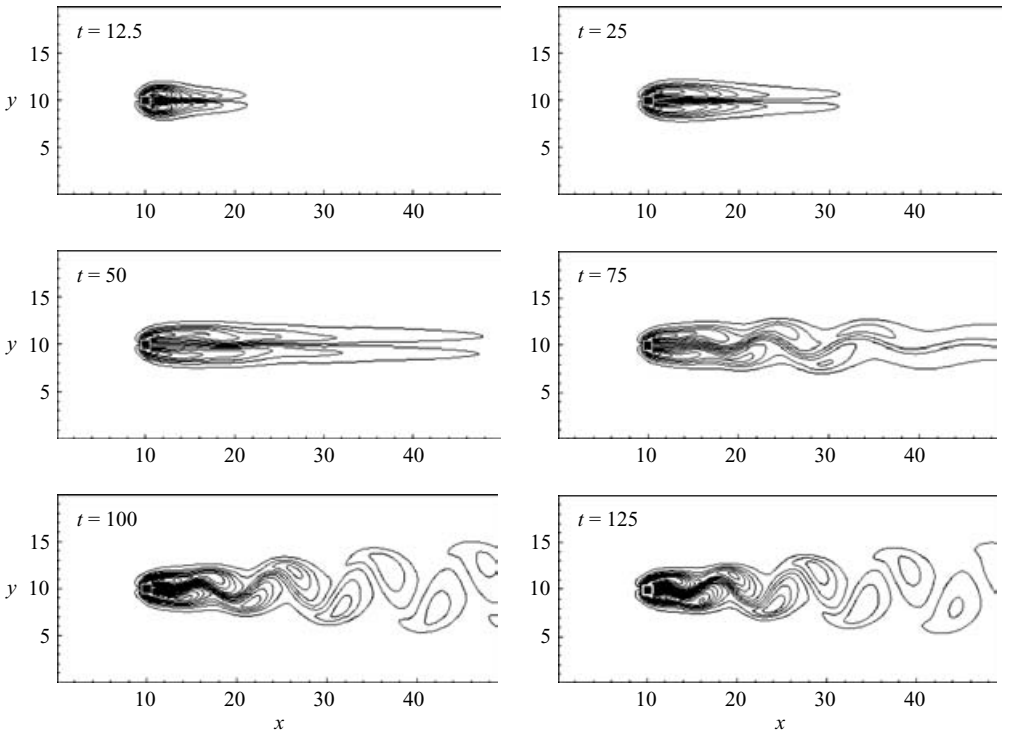



FIGURE 6. Instantaneous isolines of vorticity. $Re = 100$, $Ha = 30$, $N = 9$.

transversally to the flow. Also, the experimental blockage factor was $\beta = 0.5$, ten times bigger than the one used in the present simulations. In figure 7, instantaneous velocity fields are presented for $Ha = 30$ at the early stages of the wake formation, the last one being at a time when the vortex shedding is already established. Initially ($t = 5$), the flow is deflected in the obstacle zone. Later, a couple of counter-rotating vortices are formed inside the obstacle and in the near wake ($t = 10$). As time proceeds, vortices are first elongated ($t = 15$) and then travel downstream away from the obstacle almost without deformation. In a later time step, vortices exhibit further elongation and displacement from their symmetric original arrangement and quasi-stagnant zones are formed in the near wake. Finally, when vortex shedding appears ($t = 200$), vortices are completely displaced and the near wake is reduced, the vortices being damped within a distance of 4 units. Figure 8 shows the instantaneous isocontours of the induced magnetic field both at very early stages of development and later, when vortex shedding is well-established. The growth of the induced magnetic field zone is clearly shown, displaying up- and downstream closed loops. It can be observed that the inner loop formed behind the obstacle is 'strangled' until two well-differentiated loops with a size slightly larger than that of the obstacle are formed within the external loops. Williamson (1996) emphasized that the base suction coefficient ($-C_{pb}$) is particularly useful as a basis for discussion of the various flow regimes. Figure 9($a$) shows the base suction coefficient as a function of the Hartmann number. The inflection point in the curve observed around $Ha = 30$ separates two different dynamic behaviours. For $Ha < 30$ the Lorentz force in the obstacle zone has no transversal components and presents a uniform opposition to the oncoming flow on the central axial line; therefore, the pressure drop in the zone covered by the magnetized plates (from which $-C_{pb}$ is

https://doi.org/10.1017/S0022112006008810 Published online by Cambridge University Press

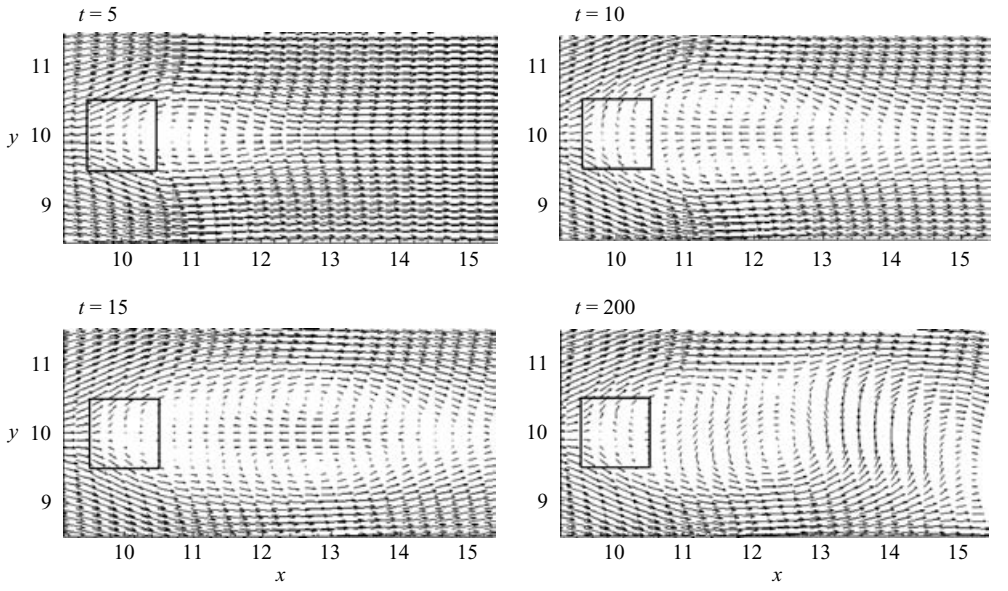



FIGURE 7. Instantaneous velocity field at the onset of vortex shedding. At $t = 200$ the periodic flow is well established. $Re = 100$, $Ha = 30$, $N = 9$.

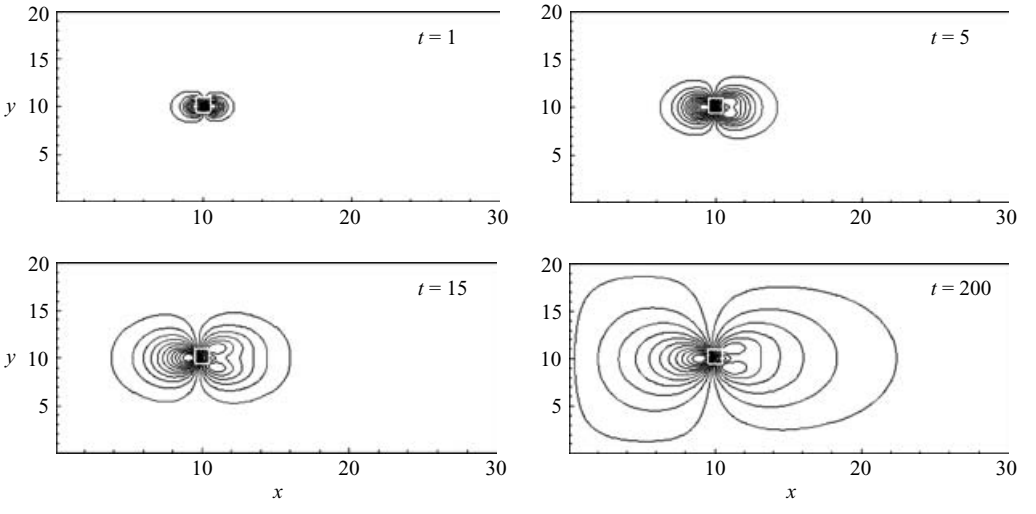



FIGURE 8. Instantaneous isocontours of induced magnetic field at the different stages of development. $Re = 100$, $Ha = 30$, $N = 9$.

calculated, see (4.5)) is rather smooth and increases with $Ha$. For $Ha > 30$, however, the pair of separated downstream inner current loops leads to the appearance of transversal components of the Lorentz force. This provokes a non-monotonic pressure drop in the square zone covered by the magnetized surfaces; the pressure increases locally at the downstream edge of the square causing a decrease of $-C_{pb}$. Figure 9($b$) shows the maximum pressure drop, $(\Delta p)_{max}$, created by the magnetic obstacle. It is calculated by taking the difference of the maximum and minimum pressures on the central axial line. The monotonic increase of $(\Delta p)_{max}$ as the Hartmann number

https://doi.org/10.1017/S0022112006008810 Published online by Cambridge University Press

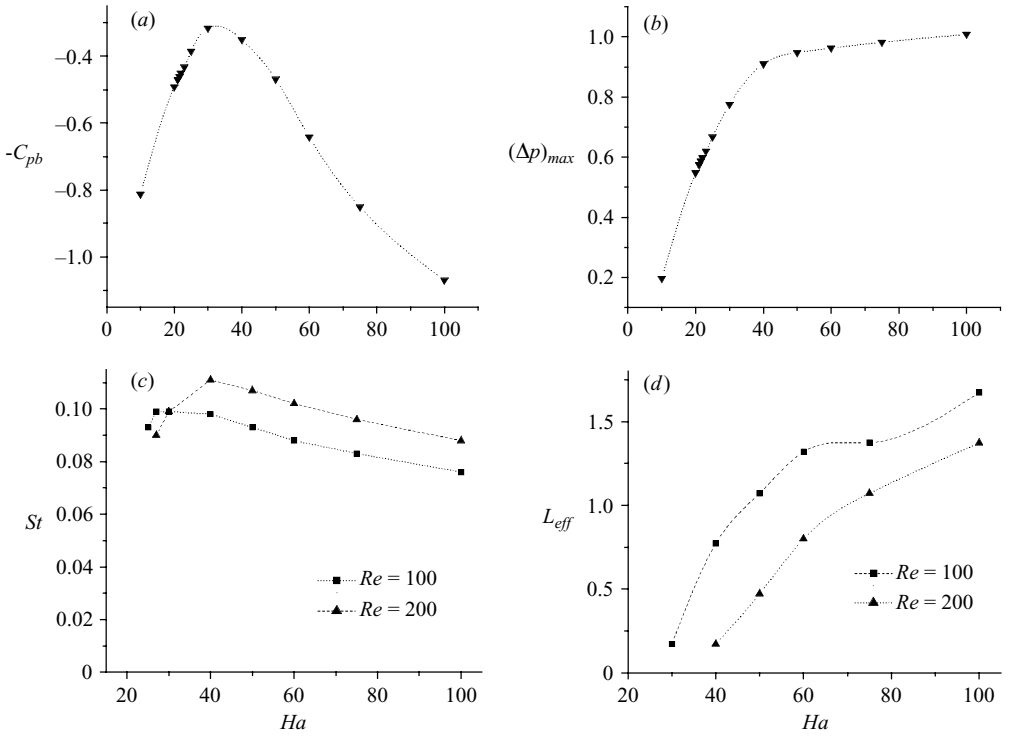



FIGURE 9. (*a*) Base pressure coefficient vs. Hartmann number. $Re = 100$. (*b*) Maximum pressure drop in the central axial line vs. Hartmann number. $Re = 100$. (*c*) Strouhal number vs. Hartmann number. (*d*) Obstacle length estimated from stagnation point vs. Hartmann number.

grows reflects the amplification of the pressure drop caused by the intensification of electromagnetic braking. The separation between the points of maximum and minimum pressure increases with the Hartmann number; for $Ha < 30$ these points are close to the borders of the square defined by the projection of the magnetized plates while for $Ha \geqslant 30$ the point of minimum pressure is displaced downstream and the separation between points of maximum and minimum pressure may be as large as 5 length units for $Ha = 100$. Although figure 9(*a*, *b*) presents instantaneous values of $-C_{pb}$ and $(\Delta p)_{max}$, these quantities display a negligible variation with time.

Two main effects are observed when the Reynolds number is increased from 100 to 200. First, the value of the Hartmann number that characterizes the onset of the periodic vortex shedding regime rises from 21.5 to 26. It corresponds to a decrease of the interaction parameter from 4.6 to 3.4. This reveals that the higher the Reynolds number, the stronger the Lorentz force required to overcome inertial effects and destabilize the flow. Second, as occurs in the flow around bluff bodies, the increase in the Reynolds number leads to a rise in the Strouhal number associated to the vortex shedding. In figure 9(*c*) the Strouhal number is shown as a function of the Hartmann number for $Re = 100$ and 200. Both curves present a similar behaviour with *Ha* and display a difference of approximately 13 % for $Ha \geqslant 40$. The Strouhal number exhibits a weak dependence on *Ha*, similarly to the behaviour observed in other MHD flows where the vortex shedding phenomenon appears (Bühler 1996; Mück *et al.* 2000). For both $Re = 100$ and 200, *St* rises to a maximum value and thereafter presents a slight decrease with *Ha*. The maximum values reached by *St* are 0.099 and 0.111 for $Re = 100$

https://doi.org/10.1017/S0022112006008810 Published online by Cambridge University Press

and 200, respectively, which are smaller than the values reported by Sohankar *et al.* (1998) (0.150 and 0.167, respectively) from two-dimensional simulations of flows around square cylinders. Notice, however, that the Reynolds number is based on the length of the magnetized plates, which has been taken as a characteristic length of the obstacle. But actually, the *effective* obstacle size depends on the Hartmann number in the sense that, for a given $Re$, the value of $Ha$ determines the extent to which the flow penetrates the obstacle. In the vortex shedding regime the Hartmann braking is strong enough to stop the flow and produce a stagnation point on the centreline upstream of the obstacle centre. Thus, an approximate estimation of the effective length, $L_{eff}$, can be given by twice the distance between the point of maximum magnetic field strength and this stagnation point. In figure 9($d$), $L_{eff}$ is plotted as a function of $Ha$ for $Re = 100$ and 200. It clearly shows that the effective length is larger the larger $Ha$ is. The initial rise of the Strouhal number as $Ha$ increases may reflect the fact that the effective Reynolds number, calculated with $L_{eff}$ instead of $L$, also increases. However, this tendency is not maintained and for Hartmann numbers larger than 30–40 the Strouhal number displays a slight (but constant) decrease. This might be a dissipative effect caused by Joule heat as the Hartmann number grows.

## 6. Conclusions

Previous investigations on MHD vortex shedding have considered the effect of a magnetic field on vortex formation and evolution. However, in these studies vortices were generated by solid obstacles or inhomogeneities in the electrical conductivity of the walls under uniform magnetic fields. For a sufficiently high magnetic field, vortices present a tendency towards two-dimensionality, with their axis parallel to the applied field and a Hartmann braking damping the motion. The flow past a magnetic obstacle presents a different scenario, that is, the creation of vortices by Lorentz forces and their evolution under conditions where magnetic field is absent or negligible.

The main objective of the present investigation is to draw attention to the possibility of producing steady and unsteady generation of vortices in non-uniform localized magnetic field distributions. This has immediate implications for heat transfer enhancement applications. The key aspect of the flow analysis is the consideration of inertial effects and the existence of electromagnetic non-uniformities given by applied magnetic field gradients. We have taken a quasi-two-dimensional approximation that introduces the effect of boundary layers through a Hartmann–Rayleigh friction term. This term models the Hartmann braking near the zone of high magnetic field strength, and transforms to a Rayleigh friction in zones where the magnetic field is negligible. However, we have considered conditions where inertial effects dominate over Hartmann–Rayleigh friction. The numerical results have shown that the problem studied in this work presents many similarities with the flow around bluff bodies, displaying steady as well as time-periodic vortical flow regimes. It is because of these similarities that the term *magnetic obstacle* has been introduced, and it appears that a scenario analogous to that found in the flow around a cylinder may arise for the flow past a magnetic obstacle. For a fixed Reynolds number, an increase in the Hartmann number reinforces the braking of the fluid in the high magnetic field zone, producing a flow around the obstacle. This causes the intensification of shear layers in the lateral fringing zones and the formation of a low-velocity (quasi-stagnant) region either inside the obstacle or in the near wake behind it. For $Re = 100$–200 either steady or time-periodic regimes are observed according to the value of the Hartmann number. For $Re = 100$ and $Ha \approx 21$, tenuous steady elongated vortices are

https://doi.org/10.1017/S0022112006008810 Published online by Cambridge University Press

formed behind the obstacle. An increase in the Hartmann number leads to self-excited wake oscillations and eventually to the establishment of a vortex shedding process. The onset of the instability appears when the interaction parameter $N$ is $O(1)$. However, the mechanism that gives rise to the appearance of vortical structures and periodic vortex shedding is clearly different from that in the flow past solid obstacles. Similarly to the MHD flow in a channel with a non-uniform electrical wall conductivity (Bühler 1996), the velocity deficit across the shear layers is the driving mechanism for instabilities. The Strouhal number characteristic of the vortex shedding is smaller than the one found in the flow around solid cylinders. As in MHD flows past solid obstacles, a weak variation of the Strouhal number with the Hartmann number was found. Besides the increase of the Hartmann number required for the onset of the instability, the increase in $Re$ does not result in any new effects except for a slight rise in the Strouhal number, an event also observed in the flow past bluff bodies. It is worth noting that the periodic vortical regime can be reached at relatively small Hartmann numbers and at Reynolds numbers at which similar phenomena are observed in the flow around solid bodies. The experiments by Honji (1991) and Honji & Haraguchi (1995) showed the possibility of obtaining vortex shedding and a wavy wake in electrolytic fluids using permanent magnets and injecting a transversal electric current. Hence, the experimental verification of the vortex shedding process under conditions similar to those of the present investigation appears to be an attainable objective.

The few cases examined here give a glimpse of what appears to be a very rich flow behaviour. Although a wider parameter study is required to establish a more detailed picture of different flow regimes, the exploration of Reynolds numbers higher than 200 has to be undertaken with caution. We have limted our calculations to $Re \leqslant 200$ in order to ensure that the flow is laminar. Higher $Re$ may result in turbulence in the far wake. In fact, this was observed in the quasi-two-dimensional flow studied by Bühler (1996). We have justified the applicability of the quasi-two-dimensional approach in the flow past a magnetic obstacle in the laminar regime, but further modifications of the model and a different computational technique may be needed if the flow is turbulent. Applicability of quasi-two-dimensional models to turbulent MHD flows under special constraints leading to two-dimensionality is currently being debated (see for instance Thess & Zikanov (2004)). The development of a numerical scheme capable of resolving three-dimensional structures and differentiating different transitional scenarios is a future task. However, since many fundamental features of the flow are retained in the quasi-two-dimensional approximation, we believe that such an approach is justified provided that the Reynolds number is $\leqslant 200$. In particular, it allows a detailed study of the wake structure and the transition between stationary and non-stationary regimes.

The first author wishes to thank the Fusion Science and Technology Center for the support received during his sabbatical stay at UCLA. Support from UC MEXUS-CONACYT Faculty Fellowship Program and DGAPA-UNAM under project IN111705 is also gratefully acknowledged.

## REFERENCES

Abdou, M. A., Ying, A., Morley, N., Gulec, A., Smolentsev, S. *et al.* 2001 On the exploration of innovative concepts for fusion chamber technology. *Fusion Engng Design* **54**, 181–247.

Alpher, A., Hurwitz, H., Johnson, R. H. & White, D. R. 1960 Some studies of free-surface mercury magnetohydrodynamics. *Rev. Mod. Phys.* **32**, 758–769.

https://doi.org/10.1017/S0022112006008810 Published online by Cambridge University Press

Bocheninskii, V. P., Branover, G. G., Tananaev, A. V. & Cheryaev, Yu. P. 1971 An experimental study of the resistance to the flow of an electroconductive fluid in plane insulated channels in the presence of a transverse magnetic field, with consideration given to the end effect and the roughness of the walls. *Izv. Akad. Nauk SSSR, Mekh. Zhidk. Gaza* **4**, 10–21.

Blackburn, H. M. & Henderson, R. D. 1999 A study of two-dimensional flow past an oscillating cylinder. *J. Fluid Mech.* **385**, 255–286.

Bruneau, Ch. H. & Fabrie, P. 1994 Effective downstream boundary conditions for incompressible Navier–Stokes equations. *Intl J. Numer Methods Fluids* **19**, 693–705.

Bühler, L. 1996 Instabilities in quasi-two-dimensional magnetohydrodynamic flows. *J. Fluid Mech.* **326**, 125–150.

Burr, U., Barleon, L., Müller, U. & Tsinober, A. 2000 Turbulent transport of momentum and heat in magnetohydrodynamic rectangular duct flow with strong side wall jets. *J. Fluid Mech.* **406**, 247–279.

Chorin, A. 1968 Numerical solutions of the Navier–Stokes equations. *Math. Comput.* **22**, 745–762.

Clercx, H. J. H., van Heijst, G. J. F. & Zoeteweij 2003 Quasi-two-dimensional turbulence in shallow fluid layers: The role of bottom friction and fluid layer depth. *Phys. Rev.* E **67**, 066303.

Couder, Y. & Basdevant, C. 1986 Experimental and numerical study of vortex couples in two-dimensional flows. *J. Fluid Mech.* **173**, 224–251.

Frank, M., Barleon, L. & Müller, U. 2001 Visual analysis of two-dimensional magnetohydrodynamics *Phys. Fluids* **13**, 2287–2295.

Griebel, M., Dornseifer T. & Neunhoeffer T. 1998 *Numerical Simulation in Fluid Dynamics.* SIAM.

Hirt, C., Nichols, B. & Romero, N. 1975 SOLA– A numerical solution algorithm for transient fluid flows. *Tech. Rep.* LA-5852. Los Alamos, NM: Los Alamos Nat. Lab.

Honji, H. 1991 Wavy wake formation in the absence of submerged bodies in electrolyzed salt water. *J. Phys. Soc. Japan* **60**, 1161–1164.

Honji, H. & Haraguchi, Y. 1995 Electrolytically induced quasi-two dimensional vortex pairs. *J. Phys. Soc. Japan* **64**, 2274–2277.

Kalyutic, A. I., Lavrent'ev, I. V. & Serebryakov, V. V. 1986 The development of flow for an electroconductive fluid in a magnetic field. *Magnetohydrodynamics* **2**, 11–14.

Kolesnikov, Y. & Tsinober, A. 1972 Two-dimensional turbulent flow behind a circular cylinder. *Magnetohydrodynamics* **3**(1), 300–307.

Lavrent'ev, I. V., Molokov, S. Yu., Sidorenkov, S. I. & Shishko, A. R. 1990 Stokes flow in a rectangular magnetohydrodynamic channel with nonconducting walls within a nonuniform magnetic field at large Hartmann numbers. *Magnetohydrodynamics* **26**(3), 328–338.

Ludford, G. S. S. 1960 The effect of a very strong magnetic cross-field on steady motion through a slightly conducting fluid. *J. Fluid Mech.* **10**, 141–155.

McCaig, M. 1977 *Permanent Magnets in Theory and Practice*. Wiley.

Moreau, R. 1990 *Magnetohydrodynamics.* Kluwer.

Mück, B., Günther, C., Müller, U. & Bühler, L. 2000 Three-dimensional MHD flows in rectangular ducts with internal obstacles. *J. Fluid Mech.* **418**, 265–295.

Müller, U. & Bühler, L. 2001 *Magnetofluiddynamics in Channels and Containers.* Springer.

Mutschke, G., Gerbeth, G., Shatrov, V. & Tomboulides, A. 1997 Two- and three-dimensional instabilities of the cylinder wake in an aligned magnetic field. *Phys. Fluids* **9**, 3114–3116.

Oertel, H. 1990 Wakes behind blunt bodies. *Annu. Rev. Fluid Mech.* **22**, 539–564.

Reed, C. B. & Picologlou, B. F. 1989 Side wall flow instabilities in liquid-metal flow under blanket relevant conditions. *Fusion Technol.* **15**, 705–715.

Satijn, M. P., Cense, A. W., Verzicco, R., Clercx, H. J. H. & van Heijst, G. J. F. 2001 Three-dimensional structure and decay properties of vortices in shallow fluid layers. *Phys. Fluids*, **13**, 1932–1945.

Sellers, C. C. & Walker, J. S. 1999 Liquid-metal flow in an electrically insulated rectangular duct with a non-uniform magnetic field. *Intl J. Engng Sci.* **37**, 541–552.

Shercliff, J. A. 1965 *Magnetohydrodynamics.* A film produced by Educational Services Inc., Watertown, Massachusetts, USA, 1965.

Smolentsev, S. 1997 Averaged model in MHD duct flow calculations. *Magnetohydrodynamics* **33**(1), 42–47.

https://doi.org/10.1017/S0022112006008810 Published online by Cambridge University Press

Sohankar, A., Norberg, C. & Davidson, L. 1998 Low-Reynolds-number flow around a square cylinder at incidence: Study of blockage, onset of vortex shedding and outlet boundary condition. *Intl J. Numer Meth. Fluids* **26**, 39–56.

Sohankar, A., Norberg, C. & Davidson, L. 1999 Simulation of three-dimensional flow around a square cylinder at moderate Reynolds numbers. *Phys. Fluids*, **11**, 288–306.

Sommeria, J. & Moreau, R. 1982 Why, how, and when, MHD turbulence becomes two-dimensional. *J. Fluid Mech.* **118**, 507–518.

Sterl, A. 1990 Numerical simulation of liquid-metal MHD flows in rectangular ducts. *J. Fluid Mech.* **216**, 161–191.

Stewartson, K. 1956 Motion of a sphere through a conducting fluid in the presence of a strong magnetc field. *Proc. Camb. Phil. Soc.* **52**, 301–316.

Talmage, G. & Walker, J. S. 1988 Three-dimensional laminar MHD flow in ducts with thin metal walls and strong magnetic fields. In *Liquid Metal Flows: Magnetohydrodynamics and Applications* (ed. H. Branover, M. Mond & Y. Unger) Progress in Astronautics and Aeronautics, vol. 111, pp. 3–25. AIAA.

Thess, A. & Zikanov, O. 2004 On the transition from two-dimensional to three-dimensional MHD turbulence. In Studying Turbulence using Numerical Simulation Data Bases. *Proc. Summer Program at the Center for Turbulence Research, Standford University and NASA Ames*, pp. 63–74.

Ting, A., Hua, T. Q., Walker, J. S. & Picologlou, B. F. 1993 Liquid-metal flow in a rectangular duct with thin metal walls and with a non-uniform magnetic field. *Intl J. Engng Sci.* **31**, 357–372.

Walker, J. S. & Picologlou, B. F. 1995 Liquid-metal flow in an insulated rectangular expansion with a strong transverse magnetic field. *J. Fluid Mech.* **309**, 111–126.

Voropayev, S. I., Afanasyev, Ya. D. & Filippov, I. A. 1991 Horizontal jets and vortex dipoles in a stratified fluid. *J. Fluid Mech.* **227**, 543–566.

Williamson, C. K. H. 1996 Vortex dynamics in the cylinder wake. *Annu. Rev. Fluid Mech.* **28**, 477–359.

Zavala Sansón, L., van Heijst, G. J. F. & Backx, N. A. 2001 Ekman decay of a dipolar vortex in a rotating fluid. *Phys. Fluids* **13**, 440–451.

Zdrakovich, M. M. 1997 *Flow around Circular Cylinders. Vol. 1: Fundamentals*. Oxford University Press.

https://doi.org/10.1017/S0022112006008810 Published online by Cambridge University Press